Structure analysis and conditions of formation of akimotoite in the Tenham chondrite

O. TSCHAUNER [iD][1*], C. MA [iD][2], C. PRESCHER[3,4], and V. B. PRAKAPENKA[3]

[1]Department of Geoscience, University of Nevada, Las Vegas, Nevada 89154–4010, USA
[2]Division of Geology and Planetary Sciences, California Institute of Technology, Pasadena, California 91125, USA
[3]Center for Advanced Radiation Sources, University of Chicago, Chicago, Illinois 60637, USA
[4]Institut für Geologie und Mineralogie, Universität zu Köln, 4705619 Köln, Germany
[*]Corresponding author. E-mail: olivert@physics.unlv.edu

Abstract–Akimotoite $(Mg,Fe)SiO_3$ is one of the most common mineralogical indicators for high-level shock metamorphism in meteorites. First described 1997, its occurrence has been amply confirmed in a number of highly shocked chondrites. Yet, a thorough structure analysis of natural akimotoite has remained extant. Here we report accurate cell parameters, fractional atomic coordinates, and site occupancies for natural akimotoite from the holotype specimen based on synchrotron microdiffraction. The variation of unit cell shape and volume with Fe content define mixing volumes. Based on the mixing volume relation for akimotoite and hemleyite, we constrain the unit cell volume of endmember hemleyite to 273.8 ± 1.0 Å^3. We show that mixing is nearly ideal for low Fe content but evolves to positive excess volume toward the Fe endmember. Based on this finding and the actual composition of akimotoite in Tenham, we show that this mineral has formed by solid–solid transformation prograde from enstatite, not by crystallization from melt.

INTRODUCTION

Akimotoite is a high-pressure polymorph of $(Mg, Fe)SiO_3$ isotypic with ilmenite. The pure Mg endmember of akimotoite has a narrow stability range above 23 GPa and at temperatures below the solidus (Ito et al. 1984; Sawamoto 1987; Ishii et al. 2011). Even mol% level amounts of $FeSiO_3$ in the bulk composition remove akimotoite from the diagram of stable phases (Ito et al. 1984; Ito and Takahashi 1989). Nevertheless, Fe-bearing akimotoite is a common phase in shock-induced melt veins in meteorites of sufficiently mafic composition such as L chondrites. It was described by Tomioka and Fujino (1997) and Sharp et al. (1997) in two independent TEM studies as naturally occurring phase and approved as a mineral by the International Mineralogical Association (Tomioka and Fujino 1999). Other occurrences were reported by TEM and Raman spectroscopic studies (Mori 1994; Xie et al. 2001; El Ohtani et al. 2004; Xie and Sharp 2004; Xie et al. 2006; Zhang 2006; Ferroir et al. 2008; Imae and Ikeda 2010; Chen and Xie 2015; Kimura et al. 2017; Feng et al. 2017). Recently, hemleyite, the endmember $FeSiO_3$ in the ilmenite structure was reported based on a solid

solution with 52 mol% $FeSiO_3$ (Bindi et al. 2017). Akimotoite is a common phase in shock-induced melt veins in heavily shocked chondrites and serves as an excellent indicator for high-grade shock states (Sharp et al. 1997; Tomioka and Fujino 1997; Ohtani et al. 2004; Xie et al. 2006, 2011; Xie and Sharp 2007; Chen and Xie 2015).

The type material of akimotoite with 79 and 21 mol% akimotoite and hemleyite, respectively, was reported to have unit cell dimensions of $a = b = 4.78$ and $c = 13.6$ Å (Tomioka and Fujino 1997, 1999), whereas $MgSiO_3$ akimotoite that was synthesized in large volume apparatus has $a = 4.728$, $c = 13.559$ Å (Horiuchi et al. 1982), and hemleyite $a = 4.7483$ and $c = 13.665$ Å (Bindi et al. 2017). Thus, the c/a ratio appears to exhibit a very pronounced reduction for the natural sample and implies a positive excess volume of 2.5 and 0.9% compared to the $MgSiO_3$ and $FeSiO_3$ endmembers, respectively. While volume differences at the percentage level do not seem large in general, for very dense structures such as akimotoite, they imply marked differences in free enthalpy. For instance, the volume difference between pure akimotoite and bridgmanite ranges only between 4 and 7% (Horiuchi

et al. 1982; Vanpeteghem et al. 2006; Boffa Ballaran et al. 2012). Thus, it is interesting to examine if the origin of the unusual composition–volume correlation in akimotoite is based in the crystal chemistry of the solid solution or in substitution mechanisms that only occur during growth under dynamic compression—or simply reflect the uncertainties of TEM-derived unit cell parameters. The higher instrumental resolution and extensive sampling of Q-space of an X-ray diffraction-based approach can address this issue.

TEM does not provide structure factor moduli that are suitable for accurate structure analysis of natural Fe-bearing akimotoite. On the other hand, synthetic solid solutions of akimotoite and hemleyite are no alternative in examining the mixing volume of this binary system: Synthesis of solid solutions under static compression has not been successful (Ito et al. 1984). Hence, we are left with a situation where the detailed structure of one of the most common and most important shock-metamorphic minerals is not well characterized and where both the detailed structure and the unit cell dimensions pose open questions. The present paper fills this gap and reports structural data for natural akimotoite from a section of the holotype specimen, the Tenham L6 chondrite.

The application of these crystal-chemical questions to the conditions in shock-induced melt veins derives directly from the answers to these questions: If solid solutions of akimotoite and hemleyite are energetically as unfavorable as the extreme positive excess volume of the previous reports suggest (Tomioka and Fujino 1997, 1999), conditions of formation and even kinetics of akimotoite are rather narrowly defined. Moreover, very Fe-rich solution may be energetically favorable through strongly negative excess volume, though they have neither been synthesized nor observed. As we will show, the mixing volume relation of the akimotoite–hemleyite system does constrain the conditions of formation of this shock-metamorphic mineral quite clearly.

SAMPLES AND METHODS

The Tenham L6 chondrite is type material for akimotoite, bridgmanite, and ringwoodite (Binns et al. 1969; Tomioka and Fujino 1997; Tschauner et al. 2014). The conditions of formation of the high-pressure phases in the shock-induced melt veins have been constrained to between 23 and 26 GPa based on the observation of bridgmanite and the liquidus of peridotitic melts (Tschauner et al. 2014). The shock effects in the minerals afar the melt veins of the Tenham chondrite indicate peak-shock pressures of at least 67–70 GPa (Stöffler et al. 1991). This offset between the apparent pressure formation of high-pressure minerals in shock-

induced melt veins and peak shock pressures assessed through the common shock-metamorphic scale (Stöffler et al. 1991) has been observed frequently. It either reflects crystallization of high-pressure phases upon release or formation along kinetic transformation boundaries rather than thermodynamic phase boundaries. A mineralogical examination of a phase with no thermodynamic stability range, like Fe-bearing akimotoite, can help to elucidate this interesting problem.

We examine the thin section TB-MC2L (USNM 7703) of the Tenham meteorite, which also contains type bridgmanite (Tschauner et al. 2014). Akimotoite occurs in shock-induced melt veins that cut through this section. The sample and the paragenesis of bridgmanite and akimotoite in Tenham has been described previously (Tomioka and Fujino 1997, 1999; Tschauner et al. 2014). Hence, we are not extensively dwelling on these aspects. Figure 1a present FE-SEM images in backscatter mode. Sampled regions of akimotoite are indicated. Figure 1b shows a high-magnification image with individual grains of akimotoite in a transformed pyroxene clast. Akimotoite was directly identified through electron backscatter diffraction (EBSD). We note that all our observations are constrained to former enstatite-rich pyroxene clasts in the melt vein. These clasts were transformed during shock into akimotoite or into akimotoite–bridgmanite mixtures. We have not found a single occurrence of akimotoite in the melt vein matrix. Figure 1c shows that the melt vein matrix is composed of two phases that occur as idiomorphic to hypidiomorphic crystallites. The brighter phase has composition $(Mg, Fe)_3Si_2O_7$ and forms crystallites with combinations of tetragonal prisms and bipyramids. This phase is currently in review as a new mineral (Ma and Tschauner 2017). The darker phase has composition $(Mg,Fe)SiO_3$ and forms platy crystallites with mostly irregular, sometimes (pseudo)-hexagonal shape. While this phase matches akimotoite by composition, its EBSD pattern does not match the akimotoite structure. In sum, we do neither observe a garnet phase nor periclase or wuestite nor akimotoite in the melt vein matrix, neither by EBSD nor by microdiffraction. The paragenesis of the melt vein matrix will be discussed in a separate paper because it is markedly different from previous suggestions and requires a complete reassessment of the structures of occurring phases. This effort is ongoing.

Electron microprobe analysis, high-resolution SEM, EBSD, and synchrotron X-ray diffraction have been used to characterize composition and structure of akimotoite. Quantitative elemental microanalyses were carried out at Caltech using a JEOL 8200 electron microprobe operated at 15 kV and 10 nA in focused beam mode. Analyses were processed with the CITZAF

correction procedure. Correlation between chemical analysis and structure was ascertained through EBSD. Analytical results are given in Table 1a. Comparative compositional analyses of the shock melt matrix are given in Table 1b. Diffraction data were collected at the undulator beamline 13-IDD (GSECARS, APS, Argonne National Laboratory; Prakapenka et al. 2008) using a primary beam energy of 30.0 keV ($\lambda = 0.4133$ Å) monochromatized by a double crystal Si 111 monochromator. The X-ray beam was focused to about 3×4 μm^2 by vertical and horizontal Kirkpatrick–Baez mirrors of 200 mm focal length. A Pilatus 3X CdTe hybrid pixel array detector was used for obtaining diffraction data. Diffraction data were collected in forward scattering geometry. A grid of sampling points was defined across the melt vein (Fig. 1a). The sample was scanned in 10 μm steps horizontally and vertically through the focused X-ray beam over the selected region. Diffraction patterns were recorded at each step. A reference background image frame was subtracted from the diffraction pattern frames thus removing the intense diffuse scattering from the glass slide of the thin section. Frame subtraction, correction for geometric distortion, and integration was conducted with the DIOPTAS software package (Prescher and Prakapenka 2015). Calibration of sample detector distance and tilt was obtained through GSE-ADA (Dera et al. 2013) and DIOPTAS.

Akimotoite was observed frequently. Other phases within the examined area were ringwoodite, taenite, pyrrhotite-5C, periclase, and bridgmanite (Fig. 2). For structure analysis, we used patterns with large phase fraction of akimotoite and low overlap of reflections with diffraction from other phases (Fig. 2). In addition, we averaged the signal of 10 such diffraction frames for maximizing powder diffraction statistics. Rietveld refinements were conducted with Powdercell (Kraus and Nolze 1996) using pseudo-Voigt profiles with the following final parameters: $U = 0.154$, $V = 0.004$, $W = 0.003$, and mixing parameters $n_a = 0.244$ and $n_b = 0$. These values are slightly different from the values reported previously for bridgmanite (Tschauner et al. 2014) because different detectors were used, but it also appears that the coherence of Bragg diffraction in akimotoite is higher: Defect density is markedly lower than in bridgmanite. Within the examined patterns, slight preferred orientation of akimotoite occurred in the (h00) zone. Rietveld refinement converged to a R_{wp} of 0.11 with a $R_{exp} = 0.02$. Quality of refinement is mostly affected by overlap with reflections from other phases within the sampled diffraction volume, notably pyrrhotite-5C is comparably coarse-grained and generated spotty diffraction patterns which are less easy to fit and increase the noise level in whole pattern refinement and extraction of structure factor moduli. Nevertheless, the structure analysis converged well: Structure factor moduli were obtained through Le Bail extraction ($R_p = 0.09$) and used for global optimization with the reversed Monte Carlo method (Putz et al. 1999). R_F converged to 0.09 (see Table 3). This result confirms that the structural assessment of akimotoite is robust.

RESULTS

Structure, Unit Cell, and Volume of Akimotoite

Unit cell and structure of two Tenham akimotoites are given in Table 2. The unit cell parameters range from $a = b = 4.736(1)$ and $c = 13.570(4)$ Å for Akim78 to 4.736(1) and 13.561(5) Å for Akim82 which gives volumes between 263.6(2) to 263.8(2) Å^3, and $c/a = 2.865(2)$ to 2.863(2). These data are based on 12 and 8 averaged diffraction patterns, respectively. We note that the EPM chemical analyses give slightly higher Fe contents than some of our Rietveld refinements. The chemical analyses are based on large transformed clasts, whereas the diffraction analysis samples akimotoite occurrences through the entire thickness of the section and over extended areas. This includes possible occurrences of sub-μm-scale crystallites in the melt vein matrix. We note that the Rietveld refinement yields on average slightly lower Fe content than EPMA. Figure 3 shows the volume of akimotoite as function of Fe content (in mol% $FeSiO_3$). Along with the endmember akimotoite (Horiuchi et al. 1982) and type hemleyite (Akim48; Bindi et al. 2017), the evolution of unit cell volume as function of Fe content is weakly quadratic but very close to linear within uncertainties

Fig. 1. a) High-resolution field-emission SEM images of the examined region of a shock-induced melt vein in the Tenham L chondrite. Brightest areas are pyrrhotite and taenite. Less bright rounded clasts are ringwoodite; darker clasts are akimotoite or akimotoite–bridgmanite aggregates. b) High-magnification SEM-BSE image of a polycrystalline aggregate of akimotoite. Sparse bright spots and aggregates on sub-μm scale do not give EBSD patterns and make no distinguishable contribution to the X-ray diffraction patterns. c) High-magnification SEM-BSE image of the paragenesis in the melt vein matrix. The melt vein matrix is composed of two phases that occur as idiomorphic to hypidiomorphic crystallites. The brighter phase (labeled "tenhamite" [Ma and Tschauner 2017]) has composition $(Mg,Fe)_3Si_2O_7$ and forms crystallites with combinations of tetragonal prisms and bipyramids. This phase has a spinelloid structure. The darker phase has composition $(Mg,Fe)SiO_3$ and forms platy crystallites with mostly irregular, sometimes (pseudo-)hexagonal shape. While this phase matches akimotoite by composition, its EBSD pattern does not match the akimotoite structure. (Color figure can be viewed at wileyonlinelibrary.com.)
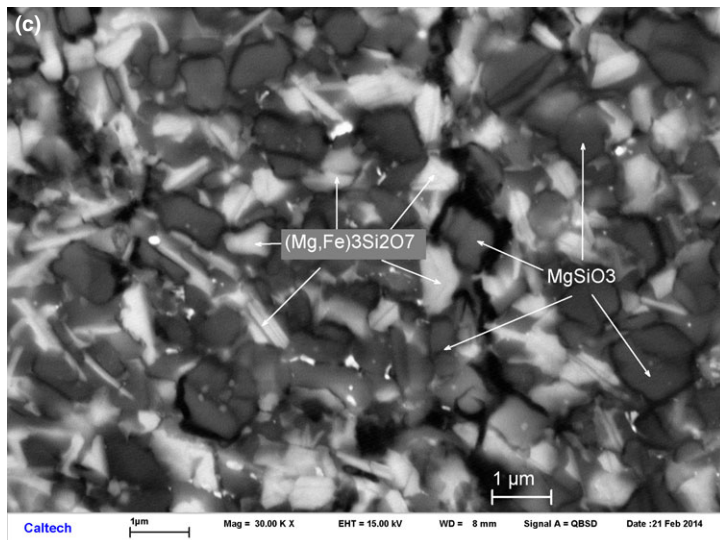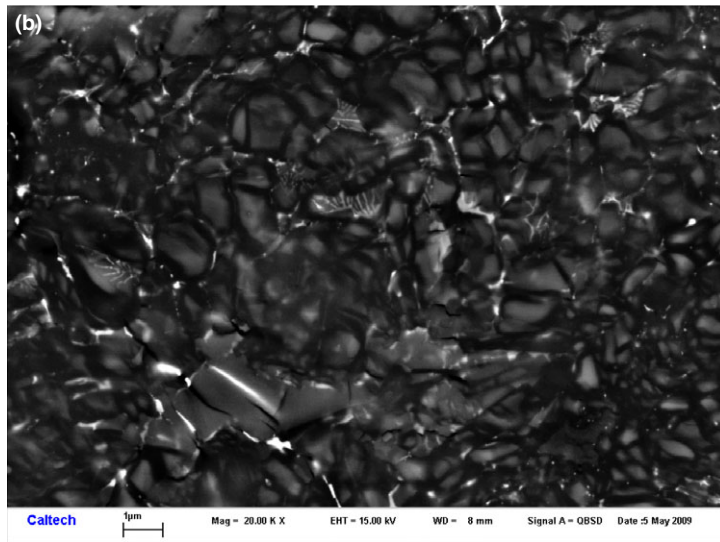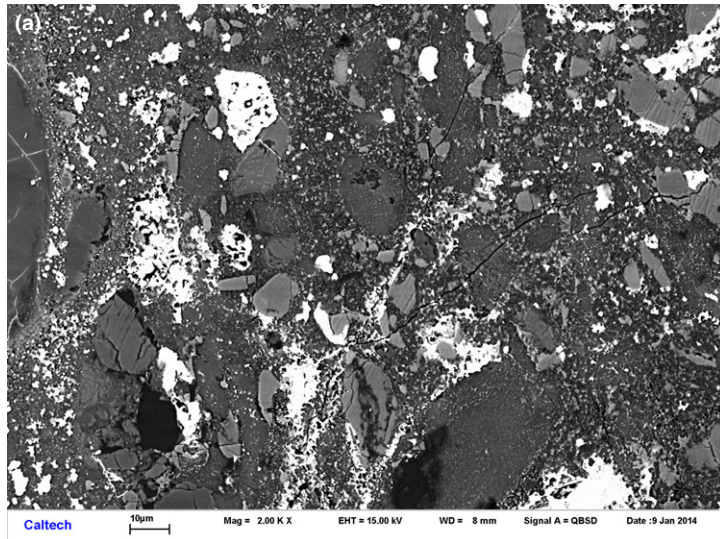
Table 1. Chemical analyses of akimotoite and melt vein matrix. (a) Akimotoite. (b) Melt vein matrix. Akimotoite was identified by EBSD prior chemical analysis. Quantitative elemental microanalyses were carried out with a JEOL 8200 electron microprobe operated at 15 kV and 10 nA in focused beam mode. Analyses were processed with the CITZAF correction procedure. Standards were anorthite (Ca), forsterite (Mg), fayalite (Fe), albite (Na), tephroite (Mn), TiO_2, Cr_2O_3, and microcline (K).

SiO_2	TiO_2	Al_2O_3	FeO	MgO	CaO	Na_2O	Cr_2O_3	MnO	Total
56.04	0.18	0.13	14.26	29.74	0.48	0.12	0.08	0.51	101.55
56.26	0.16	0.17	14.48	29.09	0.57	0.11	0.12	0.5	101.46
57.13	0.13	0.08	12.49	30.47	0.38	0.07	0.13	0.46	101.35
55.84	0.2	0.13	13.84	30.06	0.56	0.11	0.05	0.45	101.25
55.8	0.2	0.14	14.63	28.3	0.93	0.32	0.14	0.5	100.96
55	0.33	0.14	16.09	27.3	1.76	0.48	0.14	0.61	101.85
56.34	0.24	0.15	13.7	28.67	0.85	0.39	0.18	0.45	100.98
54.81	0.32	0.16	15.65	28.13	1.25	0.35	0.15	0.49	101.31
55.48	0.22	0.09	14.47	28.04	0.96	0.34	0.14	0.53	100.28
54.95	0.31	0.09	15.58	28.21	1.56	0.31	0.15	0.51	101.68
56.42	0.19	0.19	13.39	28.87	0.58	0.83	0.12	0.48	101.1
55.95	0.15	0.18	13.36	28.12	0.56	0.86	0.06	0.49	99.77
54.96	0.18	0.08	14.04	28.43	0.73	0.81	0.11	0.44	99.83
55.93	0.18	0.03	15.07	28.46	0.97	0.56	0.12	0.56	101.87
55.56	0.24	0.17	14.51	28.15	0.97	0.72	0.13	0.49	100.95
55.89	0.18	0.15	13.77	28.19	1.33	0.88	0.14	0.48	101.01
56.12	0.21	0.12	13.88	28.37	0.84	0.73	0.08	0.5	100.86
55.69	0.17	0.1	14.31	28.51	0.73	0.82	0.11	0.52	100.96
56.07	0.24	0.15	14.24	28.13	1.09	0.75	0.1	0.54	101.31
56.05	0.22	0.15	14.41	27.86	0.68	0.88	0.11	0.51	100.9
55.52	0.19	0.11	14.59	27.75	0.79	1.07	0.09	0.56	100.67
55.35	0.25	0.14	15.04	27.95	1.07	1.1	0.1	0.57	101.57
55.16	0.19	0.11	14.7	27.71	1.24	1.07	0.11	0.45	100.74
55.03	0.2	0.12	14.16	28	0.9	1	0.1	0.48	100
55.69	0.19	0.19	14.49	26.98	1.69	0.99	0.15	0.54	100.91
54.92	0.2	0.15	14.9	27.35	1.47	1.11	0.14	0.55	100.78
52.76	0.38	0.14	18.93	26.71	1.84	0.51	0.14	0.55	101.97
54.36	0.3	0.1	16.08	27.66	1.37	0.46	0.1	0.56	101
54.96	0.33	0.12	15.5	27.75	1.72	0.46	0.12	0.48	101.45
56.31	0.2	0.1	13.95	28.44	0.66	0.44	0.08	0.53	100.73
55.58	0.16	0.1	14.53	28	0.76	0.36	0.06	0.5	100.06
56.07	0.23	0.08	14.11	28.5	0.81	0.35	0.11	0.48	100.75
54.02	0.25	0.16	15.94	27.92	1.37	0.39	0.15	0.51	100.72
55.93	0.14	0.06	13.98	28.52	0.76	0.33	0.12	0.48	100.32
56.16	0.2	0.16	14.05	28.93	0.66	0.36	0.11	0.48	101.1
55.46	0.16	0.09	13.45	28.02	0.91	0.42	0.09	0.48	99.13
56.22	0.17	0.13	13.99	29.23	0.73	0.48	0.11	0.44	101.64
56.49	0.17	0.16	13.37	29.23	0.56	0.34	0.04	0.46	100.81
57.23	0.11	0.14	12.73	29.49	0.5	0.29	0.05	0.37	100.92
56.23	0.2	0.14	13.7	29.58	1.04	0.38	0.13	0.44	101.83
55.36	0.21	0.15	14.05	28.35	1.26	0.42	0.17	0.45	100.43
55.19	0.26	0.15	16.01	28.15	1.76	0.81	0.14	0.49	102.96
56.65	0.11	0.07	13.01	29.11	0.7	0.63	0.11	0.46	100.86
56.47	0.09	0.12	13.63	29.08	0.54	0.71	0.09	0.41	101.14
55.64	0.1	0.02	13.76	28.54	0.89	0.8	0.14	0.49	100.38
56.47	0.1	0.17	13.33	29.49	0.77	0.61	0.11	0.45	101.51
56.2	0.19	0.13	14.09	28.68	0.82	0.65	0.15	0.43	101.36
56.35	0.1	0.16	13.26	29.28	0.85	0.54	0.15	0.41	101.1
54.98	0.1	0.07	13.98	29.1	0.57	0.58	0.12	0.45	99.95
54.81	0.15	0.18	15.45	28.29	1.18	0.42	0.12	0.52	101.13

Table 1. *Continued.* Chemical analyses of akimotoite and melt vein matrix. (a) Akimotoite. (b) Melt vein matrix. Akimotoite was identified by EBSD prior chemical analysis. Quantitative elemental microanalyses were carried out with a JEOL 8200 electron microprobe operated at 15 kV and 10 nA in focused beam mode. Analyses were processed with the CITZAF correction procedure. Standards were anorthite (Ca), forsterite (Mg), fayalite (Fe), albite (Na), tephroite (Mn), TiO_2, Cr_2O_3, and microcline (K).

SiO_2	TiO_2	Al_2O_3	FeO	MgO	CaO	Na_2O	Cr_2O_3	MnO	Total
56.75	0.13	0.08	14.19	28.16	1.26	0.36	0.11	0.41	101.46
55.15	0.22	0.1	15.3	28.44	1.57	0.73	0.16	0.58	102.26
53.9	0.24	0.07	16.84	26.96	1.8	0.58	0.17	0.48	101.04
56.39	0.13	0.16	13.63	28.87	0.77	0.5	0.11	0.48	101.04
56.65	0.17	0.06	13.11	28.49	0.86	0.53	0.13	0.44	100.45
56.56	0.12	0.07	13.62	28.51	1.02	0.58	0.11	0.45	101.05
54.61	0.25	0.09	15.68	27.83	1.67	0.48	0.13	0.55	101.29
57.2	0.15	2.6	11.97	25.19	1.23	1.85	0.32	0.49	101.01
57.53	0.13	3.4	10.51	25.23	1.3	1.91	0.76	0.43	101.21
56.04	0.14	2.07	12.95	25.13	1.08	1.67	0.29	0.45	99.86
58.42	0.2	3.88	11.34	22.04	1.57	2.27	0.38	0.4	100.53
54.95	0.22	3.57	14.06	24.07	1.49	1.95	1.16	0.42	101.91
56.02	0.15	1.71	13.26	25.28	1.31	1.66	0.13	0.54	100.06
56.68	0.13	0.22	13.3	29.17	0.75	0.99	0.12	0.56	101.92
55.42	0.19	0.52	14.1	27.57	0.77	1.29	0.09	0.46	100.43
55.36	0.18	0.19	13.83	27.91	0.77	1.23	0.04	0.48	99.99
57.5	0.17	4.42	12.03	22.54	1.3	2.09	0.1	0.33	100.51
55.99	0.15	0.17	13.78	29.19	0.43	0.82	0.12	0.41	101.07
55.17	0.24	0.1	14.79	27.76	0.94	0.97	0.16	0.46	100.59
55.98	0.24	0.18	14.13	28.91	0.85	0.94	0.1	0.46	101.81
55.31	0.3	0.22	15.3	26.8	1.16	1.15	0.07	0.49	100.82
55.61	0.12	0.83	13.34	27.93	0.6	1.02	0.24	0.42	100.16

Point Number	SiO_2	TiO_2	Al_2O_3	FeO	MgO	CaO	Na_2O	Cr_2O_3	MnO
11	50.58	0.13	3.27	14.2	27.09	2.36	1.44	0.28	0.37
12	50.88	0.09	3.91	12.78	26.85	2.2	1.38	0.29	0.35
13	50.46	0.11	3.43	13.96	26.6	2.29	1.36	0.34	0.34
17	49.42	0.12	3.52	14.98	25.13	2.72	1.58	0.24	0.37
18	50.44	0.12	3.52	14.04	27.19	2.33	1.29	0.28	0.37
20	49.33	0.11	3.44	15.92	25.7	2.53	1.62	0.33	0.34
21	50.76	0.12	3.41	14.92	26.99	2.37	1.43	0.31	0.38
22	50.67	0.12	3.31	14.22	26.97	2.44	1.42	0.26	0.35
24	50.8	0.13	3.48	14.47	25.91	2.53	1.41	0.38	0.36
Ave	50.37	0.12	3.48	14.39	26.49	2.42	1.44	0.3	0.36
SD	0.58	0.01	0.18	0.86	0.73	0.16	0.1	0.04	0.01

(red line and blue dashed line in Fig. 3). The relation allows us to determine the unit cell volume of pure hemleyite to 273.8 ± 1.0 Å^3. The TEM data of natural akimotoite (Tomioka and Fujino 1997, 1999) give a markedly too large volume for the given composition of Akim78 (Fig. 1). We note that Ferroir et al. (2008) reported a slightly larger volume of akimotoite from Tenham for a composition similar to ours (Fig. 1). The small difference may be owed to small systematic errors such as a small zero-offset in our or in Ferroir et al.'s diffraction analysis, in the calibration of beam energy, or sample detector distance and defines the accuracy of these X-ray diffraction-based volume assessments. The

difference is comparable to the difference between ambient pressure single crystal diffraction analyses of bridgmanite (Vanpeteghem et al. 2006; Boffa Ballaran et al. 2012) and does not affect our main conclusions of nearly ideal mixing in the akimotoite–hemleyite series.

We first discuss the crystal-chemical aspects of natural akimotoite. The difference between apical and in-plane O-O distances of the SiO_6-octahedra is 0.33 Å for Ak78-82 (Table 1) and is thus indistinguishable from synthetic akimotoite100. In hemleyite (Ak48), this difference is 0.45(1) Å (Bindi et al. 2017). The octahedra in akimotoite exhibit in average some distortion in compliance with the trigonal crystal symmetry: Rather
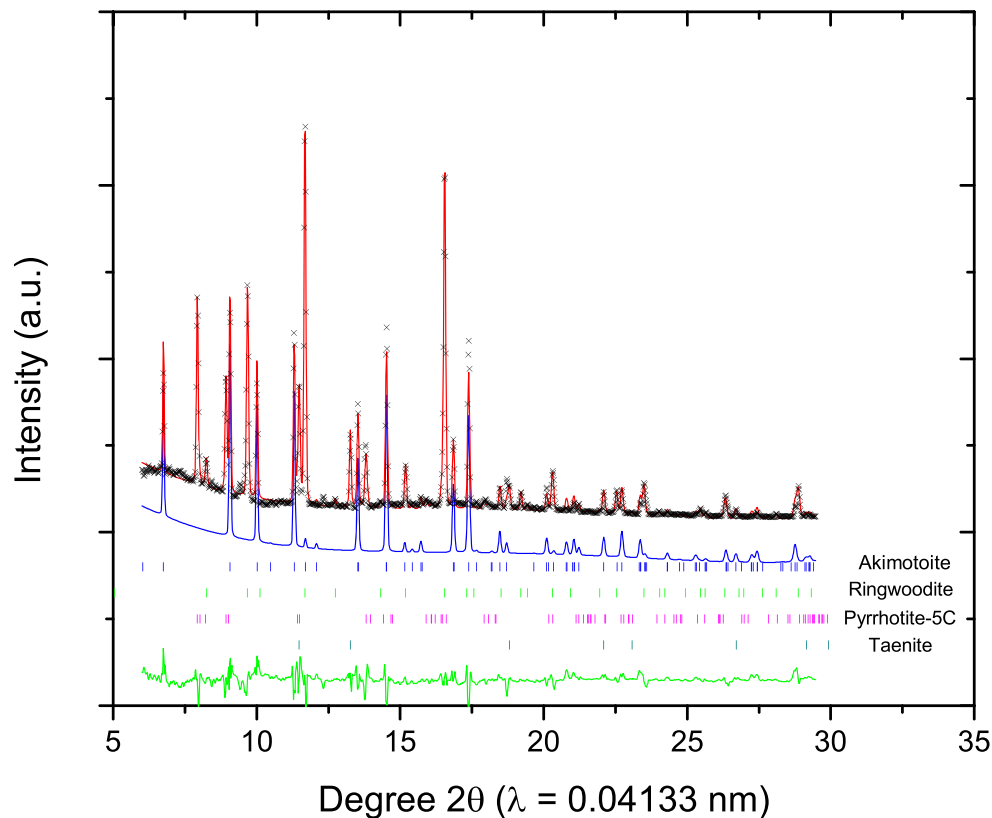
Fig. 2. Rietveld refinement of akimotoite $(Mg,Fe)SiO_3$ from holotype material of the Tenham L6 chondrite. Black crosses: Observed diffraction pattern, average over 12 patterns from different locations. Red line: Rietveld refined model pattern. The pattern includes contributions from akimotoite, ringwoodite (Rw60Ahr40), pyrrhotite-5C, and taenite. Blue: refined partial pattern of akimotoite. A constant offset was added for better visibility. Green: Residual of fit. Tick marks indicate allowed reflections of all four phases. (Color figure can be viewed at wileyonlinelibrary.com.)

than regular octahedra, they are trigonal scalenohedra. This distortion is weak but most distinct in the pseudo-octahedral base plane: In pure akimotoite, these distances range from 2.53 to 2.61 Å; in natural Ak78-82, they are 2.57(2) and 2.62(2) Å suggesting a reduction of trigonal distortion with increasing Fe content. This effect is reflected in the evolution of c/a, which shows a quadratic dependence on Fe content. As the mixing volume relation shows, substitution of Fe in akimotoite is energetically not favorable much beyond the entropic effect and generates little negative excess volume (see below). The trend of the SiO_6 units toward undistorted octrahedra is likely to be intrinsically related to this mixing behavior, as the dense and highly symmetric structure of akimotoite can compensate this polyhedral symmetrization only through volume expansion.

Finally, we note that based on our Rietveld refinements, Fe substitution on the Si-site can be nearly excluded. In addition, O-site occupancy is 100% within narrow uncertainties. This is elucidated from both chemical analysis and Rietveld refinement. Thus,

ferric iron on the Mg-site can only occur through charge balance with Na (Table 1). A correlation between Al- and Fe^{3+} content in akimotoite has been suggested (Miyajima et al. 2007). Because of the low and constant Al-content in our analyses, we cannot test this hypothesis but our findings are not inconsistent with it.

DISCUSSION

Constraints on Formation of Akimotoite in Shock-Induced Melt Veins

Akimotoite is a frequently observed high-pressure phase in shock-induced melt veins of chondrites that experienced shock states above level S5. The initial reports about the discovery of akimotoite came to contrasting conclusions about the formation of this phase through solid-state transformation of orthopyroxene (Tomioka and Fujino 1997, 1999) and crystallization from melt (Sharp et al. 1997) and this discussion has continued thereafter (Mori 1994; Xie

Table 2. Two representative structure refinements of akimotoite from Tenham. Top: Refinement for an average of ten patterns of akimotoite. Bottom: Refinement for an average of eight patterns of akimotoite with slightly lower Fe content (the lowest we have observed). The unit cell dimensions are $a = b = 4.736(1)$ and $c = 13.570(4)$ Å and $4.736(1)$ and $13.561(5)$ Å with volumes between $263.6(2)$ and $263.8(2)$ Å^3, respectively.

Atom	SFO	Wyck.	x	y	z	B
Mg	0.78 (1)	6c	0	0	0.3538 (3)	0.30 (2)
Fe	0.18 (2)	6c	0	0	0.3538 (3)	0.30 (2)
Ca	0.03[a]	6c	0	0	0.3538 (3)	0.30 (2)
Na	0.02[a]	6c	0	0	0.3538 (3)	0.30 (2)
Si	0.99 (1)	6c	0	0	0.1510 (5)	0.28 (3)
Al	0.005[a]	6c	0	0	0.1510 (5)	0.28 (3)
Fe	0.005 (2)	6c	0	0	0.1510 (5)	0.28 (3)
O	1.00 (−0.01)	18f	0.322 (2)	0.022 (2)	0.2388 (4)	0.13 (5)

Atom	SFO	Wyck.	x	y	z	B
Mg	0.82 (1)	6c	0	0	0.3536 (3)	0.30 (2)
Fe	0.16 (2)	6c	0	0	0.3536 (3)	0.30 (2)
Ca	0.03[a]	6c	0	0	0.3536 (3)	0.30 (2)
Na	0.02[a]	6c	0	0	0.3536 (3)	0.30 (2)
Si	0.99 (1)	6c	0	0	0.1514 (5)	0.28 (3)
Al	0.005[a]	6c	0	0	0.1514 (5)	0.28 (3)
Fe	0.005 (2)	6c	0	0	0.1514 (5)	0.28 (3)
O	1.00 (−0.01)	18f	0.323 (2)	0.023 (2)	0.2382 (4)	0.13 (5)

[a]Fixed.

et al. 2001; Ohtani et al. 2004; Xie and Sharp 2004; Xie et al. 2006; Zhang 2006; Ferroir et al. 2008; Imae and Ikeda 2010; Chen and Xie 2015; Kimura et al. 2017; Feng et al. 2017). Tschauner et al. (2014) reported the paragenesis of bridgmanite and akimotoite in transformed pyroxene clasts in agreement with Tomioka and Fujino (1997, 1999). However, it is not given that the occurrences in Tenham and Acfer040 (Sharp et al. 1997) are of equal formation—Acfer040 may have undergone melt crystallization upon quenching at higher pressure than the examined melt veins in Tenham, which experienced rapid quench around 20 GPa (Tschauner et al. 2014; Tomioka et al. 2016). We note that large aggregates or statistically significant occurrences of phases as dispersed nanocrystals create a signal which is measurable by synchrotron microdiffraction, as recently exemplified for growth of nanocrystalline ringwoodite and ahrensite in strained olivine of the Tissint shergottite (Ma et al. 2016). Hence, occurrences of bridgmanite and akimotoite crystallites or nanocrystals as quench phases in the Tenham melt matrix, if present at all, have to be sparse: Neither have we observed μm-scale crystallites through EBSD nor micro- or nano-crystallites through synchrotron diffraction at one of the beamlines with highest microscale flux density at high X-ray energy (Prakapenka et al. 2008). This observation argues against growth of akimotoite from melt.

However, our present data give a far better constraint on the formation of akimotoite through thermodynamics: A principal difference between akimotoite and bridgmanite is in the thermodynamic stability range. Only pure akimotoite has a stability field, whereas natural Fe-bearing akimotoite has no stability field whatsoever (Ito et al. 1984; Ito and Takahashi 1989). Under static P–T conditions, this fact already limits the formation of akimotoite to disequilibria such as initial formation of the higher entropic phase with larger volume according to Oswald's rules. This, indeed, has been proposed as a mechanism relevant for the growth of crystalline phases during shock release from fluids or melts (Tschauner et al. 2013). The mixing volume relation for akimotoite and hemleyite (Fig. 3) allows us to make a more quantitative assessment of the formation of akimotoite.

The almost linear mixing volume for akimotoite implies nearly ideal mixing, at least for the regime from Akim100 to 50. Thus, any reduction in free energy of the solid solution is almost purely entropic. This observation provides a unique tool in assessing possible crystallization of akimotoite from melt: The nearly ideal mixing between akimotoite and hemleyite implies that the Fe content of akimotoite is controlled by the activity of iron in the melt rather than in akimotoite, if akimotoite grows from melt. The average content of FeO in akimotoite is 14.17 ± 1.23 wt% (Table 1a), whereas the melt matrix has an average content of FeO

Table 3. List of calculated and observed structure factor moduli |F(hkl)| of observed reflections of akimotoite 78 (Table 2a). The observed |F(hkl)| were obtained through Le Bail extraction from the polycrystalline diffraction data. M is the multiplicity of reflections. The resulting R_F is 9% (i.e., any possible discrepancy between the structure model and real structure is <9%).

Table 3. *Continued*. List of calculated and observed structure factor moduli |F(hkl)| of observed reflections of akimotoite 78 (Table 2a). The observed |F(hkl)| were obtained through Le Bail extraction from the polycrystalline diffraction data. M is the multiplicity of reflections. The resulting R_F is 9% (i.e., any possible discrepancy between the structure model and real structure is <9%).

h	k	l	M	d(Å)	$|F_{calc}|$	$|F_{obs}|$	Δ(|F|)
−1	0	−1	6	3.926	53.9	25.5	28.4
0	−1	−2	6	3.509	386.2	286.6	99.6
−1	0	−4	6	2.613	690.1	596.2	93.9
−1	−1	0	6	2.368	501.1	423.4	77.7
0	−1	−5	6	2.262	47.3	41.2	6.1
0	0	−6	2	2.26	15.2	6.5	8.7
−2	1	−3	6	2.098	493.8	410.3	83.5
−1	−1	−3	6	2.098	591	570	21
0	−2	−1	6	2.028	124.8	125	−0.2
−2	0	−2	6	1.963	104.9	89	15.9
0	−2	−4	6	1.755	668.6	625	43.6
−1	0	−7	6	1.752	75.1	91	−15.9
−2	0	−5	6	1.636	110.9	99.5	11.4
−2	1	−6	6	1.635	919.4	924.7	−5.3
−1	−1	−6	6	1.635	595.4	579.8	15.6
0	−1	−8	6	1.567	311.5	275.5	36
−3	1	−1	6	1.54	94.5	58.9	35.6
−2	−1	−1	6	1.54	109.5	101.4	8.1
−1	−2	−2	6	1.511	105	102.7	2.3
1	−3	−2	6	1.511	226.7	205.5	21.2
0	0	−9	2	1.507	169.6	176	−6.4
−3	1	−4	6	1.41	628.8	570.7	58.1
−2	−1	−4	6	1.41	447.8	415.6	32.2
0	−2	−7	6	1.408	76.3	45.8	30.5
−3	0	0	6	1.367	960.6	1000	−39.4
−1	−2	−5	6	1.346	63.2	58.9	4.3
1	−3	−5	6	1.346	146.1	149.2	−3.1
−3	0	−3	6	1.309	79.2	66.8	12.4
0	−3	−3	6	1.309	70.3	61.5	8.8
−2	0	−8	6	1.307	137.2	135.5	1.7
−1	0	−10	6	1.288	576.1	539.3	36.8
−2	1	−9	6	1.271	78.5	102.1	−23.6
−1	−1	−9	6	1.271	419	531.4	−112.4
−3	1	−7	6	1.21	53.4	58.9	−5.5
−2	−1	−7	6	1.21	34.2	26.2	8
−2	−2	0	6	1.184	396.6	435.2	−38.6
0	−1	−11	6	1.181	68.6	64.1	4.5
−3	0	−6	6	1.17	145.3	154.5	−9.2
0	−3	−6	6	1.17	142.4	151.2	−8.8
−4	2	−3	6	1.145	236.3	210.7	25.6
−2	−2	−3	6	1.145	204.6	172.1	32.5
−1	−2	−8	6	1.144	174.5	144.6	29.9
1	−3	−8	6	1.144	191.5	156.4	35.1
−1	−3	−1	6	1.134	101.3	85.7	15.6
1	−4	−1	6	1.134	6.5	5.9	0.6
0	−2	−10	6	1.131	484.4	439.1	45.3
0	0	−12	2	1.13	304.1	274.9	29.2
−4	1	−2	6	1.122	145.3	149.2	−3.9
−3	−1	−2	6	1.122	277.2	272.9	4.3
−1	−3	−4	6	1.079	434.1	414.9	19.2
1	−4	−4	6	1.079	271.9	267.7	4.2
−2	0	−11	6	1.057	59.8	59.6	0.2
−4	1	−5	6	1.049	55.9	55.6	0.3
−3	−1	−5	6	1.049	84.7	80.5	4.2
−4	2	−6	6	1.049	379.8	375	4.8
−2	−2	−6	6	1.049	528	549.7	−21.7
−4	0	−1	6	1.023	40.6	39.3	1.3
−3	1	−10	6	1.021	356.7	334.4	22.3
−2	−1	−10	6	1.021	490.8	455.5	35.3
−2	1	−12	6	1.02	150.8	164.3	−13.5
−1	−1	−12	6	1.02	143.6	148.6	−5
0	−4	−2	6	1.014	216.9	238.9	−22
−3	0	−9	6	1.013	66.6	119.8	−53.2
0	−3	−9	6	1.013	61.6	115.2	−53.6
−1	0	−13	6	1.011	69	107.3	−38.3
−4	0	−4	6	0.982	281	295.8	−14.8
−1	−3	−7	6	0.981	83.9	81.8	2.1
1	−4	−7	6	0.981	53.2	53	0.2
−1	−2	−11	6	0.965	128.1	120.4	7.7
1	−3	−11	6	0.965	1.5	5.9	−4.4
0	−4	−5	6	0.959	24.3	20.9	3.4
−4	1	−8	6	0.945	183.3	195.7	−12.4
−3	−1	−8	6	0.945	235.9	242.8	−6.9
0	−1	−14	6	0.943	316.8	328.5	−11.7
−5	2	−1	6	0.939	113.8	109.9	3.9
−3	−2	−1	6	0.939	15.3	15.1	0.2
−2	−3	−2	6	0.932	53.6	59.6	−6
2	−5	−2	6	0.932	42.8	40.6	2.2
−4	2	−9	6	0.931	231	275.5	−44.5
−2	−2	−9	6	0.931	31.4	38	−6.6
0	−2	−13	6	0.93	14	11.1	2.9
−5	2	−4	6	0.907	324.3	369.8	−45.5
−3	−2	−4	6	0.907	370.5	431.9	−61.4
−4	0	−7	6	0.906	71.2	81.2	−10
0	0	−15	2	0.904	260.1	403.8	−143.7
−4	−1	0	6	0.895	293.4	294.5	−1.1
−1	−4	0	6	0.895	281.4	285.3	−3.9
−2	−3	−5	6	0.889	107.7	112.6	−4.9
2	−5	−5	6	0.889	14.5	12.4	2.1
−5	1	−3	6	0.878	107.2	118.5	−11.3
−4	−1	−3	6	0.878	130.1	132.9	−2.8
−1	−4	−3	6	0.878	125.8	130.2	−4.4
1	−5	−3	6	0.878	116	124.3	−8.3
0	−4	−8	6	0.877	207.2	187.2	20
−2	0	−14	6	0.876	345.9	335.7	10.2
−1	−3	−10	6	0.872	290.6	276.2	14.4

Table 3. *Continued.* List of calculated and observed structure factor moduli |*F(hkl)*| of observed reflections of akimotoite 78 (Table 2a). The observed |*F(hkl)*| were obtained through Le Bail extraction from the polycrystalline diffraction data. *M* is the multiplicity of reflections. The resulting R_F is 9% (i.e., any possible discrepancy between the structure model and real structure is <9%).

h	k	l	M	d(Å)	$|F_{calc}|$	$|F_{obs}|$	Δ(|F|)
1	−4	−10	6	0.872	411.9	392.7	19.2
−3	0	−12	6	0.871	180.9	185.2	−4.3
0	−3	−12	6	0.871	184.2	187.8	−3.6
−3	1	−13	6	0.865	31	33.4	−2.4
−2	−1	−13	6	0.865	20.7	32.1	−11.4
−5	2	−7	6	0.846	86.3	128.9	−42.6
−3	−2	−7	6	0.846	20.5	47.1	−26.6
−2	1	−15	6	0.845	92.4	104.7	−12.3
−1	−1	−15	6	0.845	73.6	136.1	−62.5
−4	1	−11	6	0.836	97.2	102.7	−5.5
−3	−1	−11	6	0.836	13.2	28.1	−14.9
−5	1	−6	6	0.832	350.7	348.2	2.5
−4	−1	−6	6	0.832	256.3	239.5	16.8
−1	−4	−6	6	0.832	268.4	248	20.4
1	−5	−6	6	0.832	343.3	343.6	−0.3
−1	0	−16	6	0.83	215.3	205.5	9.8
−2	−3	−8	6	0.823	46.1	51.7	−5.6
2	−5	−8	6	0.823	69.1	72.6	−3.5
−1	−2	−14	6	0.822	257.4	282.1	−24.7
1	−3	−14	6	0.822	284.8	316.8	−32
0	−5	−1	6	0.819	83.7	89.7	−6
−4	0	−10	6	0.818	330.2	373	−42.8
−4	2	−12	6	0.817	94.9	123	−28.1
−2	−2	−12	6	0.817	81	122.4	−41.4
−5	0	−2	6	0.814	19.7	17.7	2

of 14.39 ± 0.86 wt% (Table 1b). In other words, the Fe content of akimotoite and melt matrix is equal within uncertainty. Based on the composition, pressure, and temperature of the shock melt in Tenham, the melt is expected to contain about 1.6 times as much FeO as coexisting crystalline phases in equilibrium (Trønnes and Frost 2002). Thus, akimotoite grown from melt is expected to contain 8–9 wt% FeO. This is not observed. In addition, disequilibrium processes such as incipient chemical redistribution between melt and akimotoite (Ferroir et al. 2008) should still indicate a decrease in Fe content in akimotoite across the interface to the melt. Within the uncertainties, this is not resolved. Thus, our findings argue against the formation of akimotoite from melt. Neither the diffraction analysis nor the microchemical analysis indicates the presence of akimotoite that is markedly depleted in iron relative to the melt. This absence of a chemical signature is consistent with the lack of observation of isolated akimotoite crystals within the melt matrix in Tenham. It is also consistent with the fact that akimotoite is not a solidus phase in the MgO-SiO₂ system and is not a stable phase in the MFS system (Ito and Yamada 1982; Ito et al. 1984; Sawamoto 1987; Ishii et al. 2011). The suggestion of metastable growth of akimotoite in shock melts is no longer plausible in light of our findings of (1) ideal mixing, (2) that the composition of akimotoite is always within the range of composition of pristine enstatite-rich pyroxene in Tenham, and (3) absence of partitioning of Fe between melt and akimotoite. Thus, akimotoite is the metastable prograde transformation product of enstatite-rich clasts in Tenham and it does not grow from melt.

Finally, retrograde transformation of akimotoite out of bridgmanite is also an unlikely process: Retrograde formation of akimotoite has to be constrained to a pressure regime between 20 and 23 GPa (Tschauner et al. 2014). Moreover, it is constrained by time scale: If akimotoite–bridgmanite aggregates in transformed clasts have formed during sustained shock, it is not clear how akimotoite crystals of similar size have formed out of bridgmanite during quench on a much shorter time scale (Tschauner et al. 2014; Tomioka et al. 2016). Thus, retrograde transformation of akimotoite out of bridgmanite appears unlikely. In any case, the akimotoite–hemleyite thermodynamic mixing relation and the experimental Fe-partitioning data for dense mafic melt do not support the formation of akimotoite from melt in shock melt veins or anywhere. Formation of akimotoite from pyroxene is the only formation process that is consistent with all available observations.

SUMMARY AND CONCLUSIONS

In this study, we report the crystal structure and unit cell dimensions of natural akimotoites from material of the akimotoite holotype, the Tenham L6 chondrite. We discuss the crystal chemical effects of Fe substitution in akimotoite and obtain the mixing volume relation for akimotoite and hemleyite, constraining the unit cell volume of endmember hemleyite to 273.8 ± 1.0 Å³.

The solid solution akimotoite–hemleyite is weakly symmetric with positive excess volume at high Fe-content but close to ideal within the range of Akim50-100. This result explains the absence of ferrous akimotoite in the phase diagram of the MFS system because energetically more favorable host phases for Fe are available. Moreover, our finding implies that the occurrence of akimotoite in shock melt veins of the type material, the Tenham chondrite, is the result of prograde solid-state transformation of orthopyroxene. Crystallization from
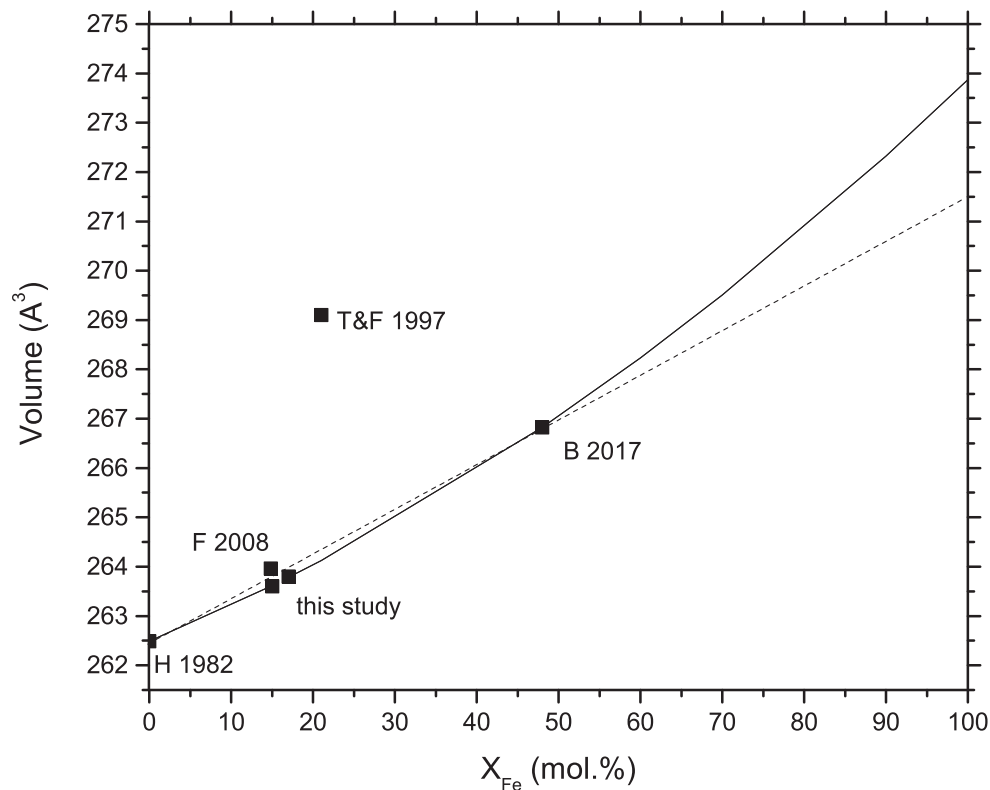
Fig. 3. Relation of unit cell volume and Fe content of akimotoite. Filled squares: measured volumes, this study. T&F: Tomioka and Fujino (1997, 1999); H: Horiuchi et al. (1982); B: Bindi et al. (2017); F: Ferroir et al. (2008). Red line: quadratic fit of the akimotoite–hemleyite join. Blue dashed line: ideal mixing line between Akim50 and 100. (Color figure can be viewed at wileyonlinelibrary.com.)

melt requires a marked depletion of akimotoite in Fe, which is not observed. The partitioning of Fe and relative depletion of akimotoite relative to melt and precursor enstatite are the decisive criteria for growth from melt. Incipient redistribution of elements at the rim of akimotoite grains is possible, though not resolved, in our study. Consistent with this finding, we have not observed akimotoite in the matrix of the shock-generated melt vein of the Tenham L6 chondrite. All observations were in transformed pyroxene clasts.

Editorial Handling—Dr. Dieter Stoeffler

REFERENCES

Bindi L., Chen M., and Xie X. 2017. Discovery of the Fe-analogue of akimotoite in the shocked Suizhou L6 chondrite. *Scientific Reports* 7:42674.

Binns R. A., Davis R. J., and Reed S. J. B. 1969. Ringwoodite, natural (Mg, Fe)$_2$SiO$_4$ spinel in the Tenham meteorite. *Nature* 221:943–944.

Boffa Ballaran T., Kurnosov A., Glazyrin K., Frost D. J., Merlini M., Hanfland M., and Caracas R. 2012. Effect of chemistry on the compressibility of silicate perovskite in the lower mantle. *Earth and Planetary Science Letters* 333:181–190.

Chen M. and Xie X. D. 2015. Shock-produced akimotoite in the Suizhou L6 chondrite. *Science China—Earth Science* 58:876–880.

Dera P, Zhuravlev K., Prakapenka V., Rivers M. L., Finkelstein G. J., Grubor-Urosevic O., Tschauner O., Clark S. M., and Downs R. T. 2013. High pressure single-

crystal micro X-ray diffraction analysis with GSE_ADA/RSV software. *High Pressure Research* 33:466–484.

Feng L., Miyahara M., Nagase T., Ohtani E., Hu S., El Goresy A., and Lin Y. 2017. Shock-induced P-T conditions and formation mechanism of akimotoite-pyroxene glass assemblages in the Grove Mountains (GRV) 052082 (L6) meteorite. *American Mineralogist* 102:1254–1262.

Ferroir T., Beck P., Van de Moortèle B., Bohn M., Reynard B., Simionovici A., El Goresy A., and Gillet P. 2008. Akimotoite in the Tenham meteorite: Crystal chemistry and high-pressure transformation mechanisms. *Earth and Planetary Science Letters* 275:26–31.

Horiuchi H., Hirano M., Ito E., and Matsui Y. 1982. $MgSiO_3$ (ilmenite-type): Single crystal X-ray diffraction study. *American Mineralogist* 67:788–793.

Imae N. and Ikeda Y. 2010. High-pressure polymorphs of magnesian orthopyroxene from a shock vein in the Yamato-000047 lherzolitic shergottite. *Meteoritics & Planetary Science* 451:43–54.

Ishii T., Kojitani H., and Akaogi M. 2011. Post-spinel transitions in pyrolite and Mg_2SiO_4 and akimotoite-perovskite transition in $MgSiO_3$: Precise comparison by high-pressure high-temperature experiments with multi-sample cell technique. *Earth and Planetary Science Letters* 309:185–197.

Ito E. and Takahashi E. 1989. Postspinel transformations in the system Mg_2SiO_4–Fe_2SiO_4 and some geophysical implications. *Journal of Geophysical Research* 94:10,637–10,646.

Ito E. and Yamada H. 1982. Stability relations of silicate spinels, ilmenites and perovskites. In *High pressure research in mineral physics*, edited by Akamoto S. and Manghnani M. H. Tokyo: Terra Sci. pp. 405–419.

Ito E., Takahashi E., and Matsui Y. 1984. The mineralogy and chemistry of the lower mantle: An implication of the ultrahigh-pressure phase-relations in the system MgO-FeO-SiO_2. *Earth and Planetary Science Letters* 67:238–248.

Kimura M., Chen M., Yoshida Y., El Goresy A., and Ohtani E. 2017. Back-transformation of high-pressure phases in a shock melt vein of an H-chondrite during atmospheric passage: Implications for the survival of high-pressure phases after decompression. *Earth and Planetary Science Letters* 217:141–150.

Kraus W. and Nolze G. 1996. POWDER CELL—A program for the representation and manipulation of crystal structures and calculation of the resulting X-ray powder patterns. *Journal of Applied Crystallography* 29:301–303.

Ma C. and Tschauner O. 2017. Proposal for the new mineral $(Mg,Fe)_3Si_2O_7$ (IMA 2017-093), submitted to the IMA-CNMNC for approval in September 2017.

Ma C., Tschauner O., Beckett J. R., Liu Y., Rossman G. R., Sinogeikin S. V., Smith J. S., and Taylor L. A. 2016. Ahrensite, gamma-Fe_2SiO_4, a new shock-metamorphic mineral from the Tissint meteorite: Implications for the Tissint shock event on Mars. *Geochimica et Cosmochimica Acta* 184:240–256.

Miyajima N., El Goresy A., Dupas-Bruzek C., Seifert F., Rubie D. C., Chen M., and Xie X. 2007. Ferric iron in Al-bearing akimotoite coexisting with iron-nickel metal in a shock-melt vein in an L-6 chondrite. *American Mineralogist* 92:1545–1549.

Mori H. 1994. Shock-induced phase transformations of the Earth and planetary materials. *Journal of the Mineralogical Society of Japan* 23:171–178.

Ohtani E., Kimura Y., Kimura M., Takata T., Kondo T., and Kubo T. 2004. Formation of high-pressure minerals in shocked L6 chondrite Yamato 791384: Constraints on shock conditions and parent body size. *Earth and Planetary Science Letters* 227:505–515.

Prakapenka V. B., Kubo A., Kuznetsov A., Laskin A., Shkurikhin O., Dera P., Rivers M. L., and Sutton S. R. 2008. Advanced flat top laser heating system for high pressure research at GSECARS: Application to the melting behavior of germanium. *High Pressure Research* 28:225–235.

Prescher C. and Prakapenka V. B. 2015. DIOPTAS: A program for reduction of two-dimensional X-ray diffraction data and data exploration. *High Pressure Research* 35:223–230.

Putz H., Schön J. C., and Jansen M. 1999. Combined method for ab initio structure solution from powder diffraction data. *Journal of Applied Crystallography* 32:864–870.

Sawamoto H. 1987. Phase diagram of $MgSiO_3$ at pressures up to 24 GPa and temperatures upto 2200°C: Phase stability and properties of tetragonal garnet. In *High pressure research in mineral physics*, edited by Manghnani M. and Syono Y. Geophysical Monographic Series, vol. 39. Washington, D.C.: AGU. pp. 209–219.

Sharp T. G., Lingemann C. M., Dupas C., and Stöffler D. 1997. Natural occurrence of $MgSiO_3$-ilmenite and evidence for $MgSiO_3$-perovskite in a shocked L chondrite. *Science* 280:352–355.

Stöffler D., Keil K., and Scott E. R. D. 1991. Shock metamorphism of ordinary chondrites. *Geochimica et Cosmochimica Acta* 55:3845–3867.

Tomioka N. and Fujino K. 1997. Natural $(Mg, Fe)SiO_3$-ilmenite and -perovskite in the Tenham meteorite. *Science* 277:1084–1086.

Tomioka N. and Fujino K. 1999. Akimotoite, $(Mg, Fe)SiO_3$, a new silicate mineral of the ilmenite group in the Tenham chondrite. *American Mineralogist* 84:267–271.

Tomioka N., Miyahara M., and Ito M. 2016. Discovery of natural $MgSiO_3$ tetragonal garnet in a shocked chondritic meteorite. *Science Advances* 25:e1501725.

Trønnes R. G. and Frost D. J. 2002. Peridotite melting and mineral-melt partitioning of major and minor elements at 22-24.5 GPa. *Earth and Planetary Science Letters* 197:117–131.

Tschauner O., Luo S.-N., Chen Y. J., McDowell A., Knight J., and Clark S. M. 2013. Shock synthesis of lanthanum-III-pernitride. *High Pressure Research* 33:202–207.

Tschauner O., Ma C., Beckett J. R., Prescher C., Prakapenka V. B., and Rossman G. R. 2014. Discovery of bridgmanite, the most abundant mineral in Earth, in a shocked meteorite. *Science* 346:1110–1112.

Vanpeteghem C. B., Zhao J., Angel R. J., Ross N. L., and Bolfan-Casanova N. 2006. Crystal structure and equation of state of $MgSiO_3$ perovskite. *Geophysical Research Letters* 33:L03306.

Xie X. D., Chen M., and Wang D. Q. 2001. Shock-related mineralogical features and P-T history of the Suizhou L6 chondrite. *European Journal of Mineralogy* 13:1177–1190.

Xie X. D., Sun Z. Y., and Chen M. 2011. The distinct morphological and petrological features of shock melt

veins in the Suizhou L6 chondrite. *Meteoritics & Planetary Science* 46:459–469.

Xie Z. D., Sharp T. G., and DeCarli P. S. 2006. High-pressure phases in a shock-induced melt vein of the Tenham L6 chondrite: Constraints on shock pressure and duration. *Geochimica et Cosmochimica Acta* 70:504–515.

Xie Z. and Sharp T. G. 2004. High-pressure phases in shock-induced melt veins of the Umbarger L6 chondrite: Constraints of shock pressure. *Meteoritics & Planetary Science* 391:2043–2054.

Xie Z. and Sharp T. G. 2007. Solid state transformation in a shock-induced melt vein of Tenham L6 chondrite. *Earth and Planetary Science Letters* 254:433–445.

Zhang A. C. 2006. Pyroxene polymorphs in melt veins of the heavily shocked Sixiangkou L6 chondrite. *European Journal of Mineralogy* 18:719–726.